Role of the Barrel Shock as Control Element for Hypersonic Transverse Jet Injection Flows

Ravichandra Srinivasan* and Rodney D. W. Bowersox†
Aerospace Engineering, Texas A&M University, College Station, TX 77843

The role of the barrel shock in controlling the secondary flow associated with gaseous injection of underexpanded air through circular and 15-degree half-angle diamond orifices into a high Reynolds number Mach 5.0 freestream was numerically investigated. The Detached-Eddy-Simulation version of Menter's two-equation SST model was used in these simulations. A discussion of the resulting flowfield with emphasis on the structure of the barrel shock and its effect on the flow is presented. A new *transverse* counter rotating vortex pair with the potential to act a gasdynamic flame holding mechanism was identified in the flow. The results were also post-processed to identify the salient vorticity transport processes.

Nomenclature

d	=	jet diameter
p	=	pressure
T	=	temperature
M	=	Mach number
δ	=	boundary layer thickness
Re	=	Reynolds number
$\vec{\omega}$	=	vorticity vector
$\vec{V}$	=	velocity vector
ρ	=	density
ϕ	=	representative scalar
Π	=	$\Pi^L + \Pi^T$, laminar and turbulent stress tensors
μ	=	dynamic viscosity
λ	=	second viscosity, $-(2/3)\,\mu$

I. Introduction

RENEWED interest[1,2] in air-breathing hypersonic vehicles for military and civilian use has prompted a surge in research of related technologies. Numerous challenges have to be overcome in order to achieve the goal of hypersonic flight. First, for airbreathing propulsion powered systems, the predicted thrust margins are small[3]. Hence, efficient fuel injection, flame holding and drag reduction are of paramount importance. Second, the external and internal skin temperatures are extreme. Thus, robust and low drag thermal management and reaction control are also vital. In order to overcome these challenges, new methods in high-speed flow control are required.

Current hypersonic flow control research has mainly focused on the utilization of magneto-hydrodynamic and plasma effects[4-8]. Plasmas have been show to affect flow characteristics due to induced thermal effects[4-6]. They also have the ability to provide ignition at low mean temperatures, control inlet flow and shock position.[7] Focused energy deposition ahead of high-speed vehicles has been shown to reduce wave drag by as much as 50 percent[8]. It can also help in short duration reduction of peak pressure and increase heat transfer characteristics[9]. Deposition off the stagnation streamline induces lift and pitching moment[8]. Magneto-Hydrodynamic effects can be used to move the

* Graduate Research Assistant, Aerospace Engineering, Student Member AIAA.
† Associate Professor, Aerospace Engineering, Associate Fellow AIAA.

inlet shock back and forth to accommodate for off-design flight conditions. Control of internal flow through MHD can result in an increase in specific impulse[10]. Also, MHD effects have been found to be most significant in the boundary layer and not so much in the core high-speed flow[11].

Fluidic control (e.g., boundary layer bleed and or injection) have proven useful. For example, an aerodynamic ramp concept[12] has been investigated with the goal of increasing penetration and mixing within a scramjet. Helium injection through slots has been used to achieve structural reorganization of hypersonic boundary layers[13,14]. The current leading candidate for flame holding within scramjets is the wall cavity flame concept[15,16]. This concept has proven effective, however, the cavity induces flow unsteadiness and the cavity has to endure a very harsh environment.

Jet injection has the potential to address many of the above mentioned challenges associated with hypersonic flight. Often, the requirements are conflicting. For example, the requirements for fuel injection include weak shocks for reduced drag and recirculation, enhanced vorticity for mixing and increased penetration for fuel dispersion. However, fluidic control of drag and or heat transfer requires reduced vorticity and penetration to maintain the cooling fluid near the surface. Reaction control jet application requires strong shocks and the associated high-pressure recirculation regions to generate force amplification.

The flowfield generated by transverse injection into a high-speed flow has been the subject of numerous investigations[17-21]. The flow field generated by injection through a circular orifice is show in Fig. 1[22]. As indicated the flow is characterized by numerous shocks and secondary flow structures. The first flow feature encountered in the streamwise direction is the interaction or bow shock produced as a result of the freestream impacting on the injector streamtube. For injector configurations, where δ/d is on the order of one or more, a separation region and lambda shock form upstream of the injector port. A horseshoe vortex forms between the jet and the interaction shock. After entering the freestream, the underexpanded jet undergoes a rapid Prandtl-Meyer expansion surrounded by a barrel shock. A shock wave normal to the jet path known as the Mach disk, terminates the barrel shock, and compresses the flow to the effective back-pressure. Downstream of the Mach disk, a counter rotating vortex pair forms within the jet plume. Wake vortices are also formed. The plume vorticity and turbulent mechanisms induce the required large scale mixing between the jet fluid and the freestream.

The objective for the present study was to characterize the influence of the barrel shock on the near field secondary flow structure associated with injection into a hypersonic freestream. Specifically, the role of the barrel shock in controlling the secondary flow associated with gaseous injection of underexpanded air through circular and 15-degree half-angle diamond orifices into a high Reynolds number Mach 5.0 freestream was numerically investigated. The Detached-Eddy-Simulation (DES) version of Menter's two-equation SST model was used in these simulations. In these simulations, it was discovered that the barrel shock can be tailored to produce a new *transverse* counter rotating vortex pair in the jet interaction near-field. This vortex pair has the potential to act as a flame holding device in scramjets. A discussion of the resulting flowfield with emphasis on the structure of the barrel shock and its effect on the flow is presented. The results were also post-processed to identify the salient vorticity transport processes.

II. Numerical Simulations

The following sections provide details of the geometry, grid generation, boundary conditions, and simulation.

A. Geometry

The domain used in the simulation is that of experiments conducted by Bowersox et al[20]. Figure 2 is an illustration of the coordinate system and test section. Freestream conditions are listed in Table 1. The diamond injector port with a half angle of 15° was used. The half angle was arbitrarily chosen with the goals of (1) weak leading edge shock and (2) minimization of tunnel wall reflections. Although five different incidence angles were investigated, only results from the 90° injection are discussed in this paper. The injector port has an area of 18.8 mm^2 with an effective diameter of 4.89 mm. The leading edge of the injector was located 7.14 cm downstream of the tunnel inlet. The total pressure of the injectant was 0.10 MPa and the total temperature was 295.0 K. The exit

Table 1. Freestream Conditions.

Mach	P_t (MPa)	T_t (K)	Re/m ($x10^6$)	δ (mm)
5.0	2.4	360	53.0	8.3

Mach number of the jet was approximately 1.0. Simulations were also performed with a circular injector having the same effective diameter as the diamond injector.

B. Grid Generation

Unstructured grids were generated using VGRID[23]. Figures 3a, 3b and 3c show cross-sectional planes of the grid in the x, y and z directions. The initial grid was composed of tetrahedrons. The grid preprocessor provided with Cobalt converts tetrahedral cells in the boundary layer to prisms in order to reduce the total cell count. Four different grids were generated for the simulation involving the diamond shaped injector and three grids were used for the circular injector case. Grids were refined using manual as well as automated techniques. Results discussed here were obtained by using the grid that was refined using automated techniques. The total number of cells in the grid, after refinement, was approximately 6.0 million. The cells in the boundary layer were such that $y^+ < 1.0$ at the first cell off the wall. The height of the computational domain was restricted to y/d = 7.78 since all flow features of interest occur within this height. The entire lateral width of the experimental domain, i.e. z/d = ± 7.78 was modeled.

C. Boundary Conditions

At the inlet of the domain a velocity profile with an incoming boundary layer was specified. The thickness of the boundary layer matches the experimental value. Adiabatic no slip conditions were applied at the tunnel floor and injector port wall. Tangency boundary conditions were applied at the tunnel sidewalls. Extrapolation was used at the exit and at the top surface of the domain. Velocity, static pressure and density were specified at the injector inlet.

D. Simulation

The Cobalt[24] flow solver was used to simulate the flow. Cobalt is a cell centered, unstructured CFD code with the ability to solve both Euler and Reynolds Averaged Navier-Stokes (RANS) equations in integral form with second order accuracy in both space and time. It has a suite of turbulence models including the one-equation Spalart-Allmaras and two-equation Menter's SST and Wilcox's *k*-ω. DES versions of the Spalart-Allmaras and Menter's SST models are also available. Menter's SST with DES[25,26] was used in the current work. Initial iterations were executed using the laminar form of the Navier-Stokes equations. The solution was restarted with Menter's SST turbulence model. After convergence, the solution was restarted with the DES form of the two-equation model. Initial DES iterations were executed without any averaging in order to avoid transient flow features. Time averaging was then enabled and the solution continued until there was negligible change in averaged results. Grid convergence studies were conducted using four different grids. The criteria used for grid convergence were wall pressure and percentage of resolved turbulent kinetic energy. Time step convergence was conducted using two different time steps. Table 2 lists details of the calculation including iterations, models and time steps used. The simulations were executed on supercomputers at Aeronautical Systems Center (ASC), one of the Major Shared Resource Centers (MSRC).

Table 2. Simulation Details.

Run	Model	Iterations	Time Step
90 Degree Diamond and Circular Injectors.	Laminar	1000	CFL
	Two-Equation	2000	CFL
	DES-Two-Equation	3000	1.0E-6
	Averaged DES-Two-Equation	6000	1.0E-6

III. Compressible Vorticity Transport Equation

The compressible form of the vorticity transport equation is obtained by taking the curl of the Favre-averaged form of the Navier-Stokes equations. Using the conservation of mass relation and vector identities in the resulting equation we obtain

$$\frac{D\bar{\omega}}{Dt} = -\bar{\omega}\left(\nabla\cdot\vec{V}\right) + \left(\bar{\omega}\cdot\nabla\right)\vec{V} + \left[\frac{(\nabla\rho)\times(\nabla p)}{\rho^2}\right] + \frac{1}{\rho}\nabla\times\left(\nabla\cdot\bar{\bar{\Pi}}\right) - \left[\frac{(\nabla\rho)\times\left(\nabla\cdot\bar{\bar{\Pi}}\right)}{\rho^2}\right] \quad (1)$$

where,

$$\Pi = \Pi_{ij}^{L} + \Pi_{ij}^{T} \tag{2}$$

$$\Pi_{ij}^{L} = \mu\left(\frac{\partial u_i}{\partial x_j} + \frac{\partial u_j}{\partial x_i}\right) + \lambda\delta_{ij}\nabla.\vec{V} \tag{3}$$

and

$$\Pi_{ij}^{T} = \overline{\overline{\rho u_i u_j}} \tag{4}$$

The x-component of this vector equation is given by

$$\begin{aligned}\left\{\bar{V}_x\frac{\partial\bar{\omega}_x}{\partial x} + \bar{V}_y\frac{\partial\bar{\omega}_x}{\partial y} + \bar{V}_z\frac{\partial\bar{\omega}_x}{\partial z}\right\} &= \left\{-\bar{\omega}_x\frac{\partial\bar{V}_x}{\partial x} - \bar{\omega}_x\frac{\partial\bar{V}_y}{\partial y} - \bar{\omega}_x\frac{\partial\bar{V}_z}{\partial z}\right\} \\ &+ \left\{\bar{\omega}_x\frac{\partial\bar{V}_x}{\partial x} + \bar{\omega}_y\frac{\partial\bar{V}_x}{\partial y} + \bar{\omega}_z\frac{\partial\bar{V}_x}{\partial z}\right\} \\ &+ \left\{\frac{1}{\rho^2}\left[\frac{\partial\rho}{\partial y}\frac{\partial p}{\partial z} - \frac{\partial\rho}{\partial z}\frac{\partial p}{\partial y}\right]\right\} \\ &+ \left\{\frac{1}{\rho}\left[\frac{\partial T_3^L}{\partial y} - \frac{\partial T_2^L}{\partial z}\right]\right\} + \left\{\frac{1}{\rho}\left[\frac{\partial T_3^T}{\partial y} - \frac{\partial T_2^T}{\partial z}\right]\right\} \\ &- \left\{\frac{1}{\rho^2}\left[T_3^L\frac{\partial\rho}{\partial y} - T_2^L\frac{\partial\rho}{\partial z}\right]\right\} - \left\{\frac{1}{\rho^2}\left[T_3^T\frac{\partial\rho}{\partial y} - T_2^T\frac{\partial\rho}{\partial z}\right]\right\}\end{aligned} \tag{5}$$

where,

$$T_i^L = \frac{\partial\bar{\bar{\Pi}}_{ji}^{L}}{\partial x_j} \quad ; \quad T_i^T = \frac{\partial\bar{\bar{\Pi}}_{ji}^{T}}{\partial x_j} \tag{6}$$

The terms in equation (5) are grouped using braces. The term on the left hand side of equation (5) represents vorticity convection. The first term on the right had side is the compressibility term since this would be zero in incompressible flows. The second and third terms denote three-dimensional vortex stretching and baroclinic torque. The fourth and fifth terms represent laminar and turbulent anisotropic torque while the sixth and seventh terms represent laminar and turbulent stress torque.

A FORTRAN program was written to compute the terms in Eq. (1) . The inputs for the program were the grid file and time averaged solution output. The following time averaged values were used in the program; (a) density, (b) velocity components, (c) pressure and (d) Reynolds stress tensor components. Solution results were stored at grid points within the domain. Time averaged temperature was calculated using the ideal gas relation and dynamic viscosity was calculated using Sutherland's law. The derivative of a scalar variable at a node was evaluated using a least squares method[27] which depends on the solution value at all neighboring nodes. The procedure for evaluating the gradient is as shown below.

Let ϕ be any scalar function whose gradient, $\nabla\phi$, we want to evaluate at any node denoted by *a* (Fig. 4). The neighbor nodes, *j*, are those used in evaluating the gradient. The value of the scalar variable at j is given by

$$\phi_j = \phi_a + \nabla\phi \cdot \left(\vec{r}_j - \vec{r}_a\right) \tag{7}$$

A new relation is formed to estimate value of the scalar at node *j* as shown

$$\phi'_j = \phi_a + \nabla\phi \cdot \left(\vec{r}_j - \vec{r}_a\right) \tag{8}$$

Since the value of the scalar ϕ is already know from the CFD solution The gradient is evaluated by minimizing the distance between ϕ_j and ϕ'_j. This leads to a matrix system

$$\mathbf{Ax = B} \tag{9}$$

where $\mathbf{A}$ is the matrix of coefficients given by

$$\begin{bmatrix} \sum_j \Delta x_{ja}\Delta x_{ja} & \sum_j \Delta x_{ja}\Delta y_{ja} & \sum_j \Delta x_{ja}\Delta z_{ja} \\ \sum_j \Delta y_{ja}\Delta x_{ja} & \sum_j \Delta y_{ja}\Delta y_{ja} & \sum_j \Delta y_{ja}\Delta z_{ja} \\ \sum_j \Delta z_{ja}\Delta x_{ja} & \sum_j \Delta z_{ja}\Delta y_{ja} & \sum_j \Delta z_{ja}\Delta z_{ja} \end{bmatrix} \tag{10}$$

$\mathbf{x}$ is the vector of components of the scalar gradient.

$$\mathbf{x} = \begin{bmatrix} \phi_x \\ \phi_y \\ \phi_z \end{bmatrix} \tag{11}$$

The RHS vector $\mathbf{B}$ is given by

$$\mathbf{B} = \begin{bmatrix} \sum_j \Delta x_{ja}\Delta\phi_{ja} \\ \sum_j \Delta y_{ja}\Delta\phi_{ja} \\ \sum_j \Delta z_{ja}\Delta\phi_{ja} \end{bmatrix} \tag{12}$$

The solution is given by

$$\mathbf{x = A^{-1}B} \tag{13}$$

The inverse of the coefficient matrix was evaluated using the relation

$$\mathbf{A^{-1}} = \frac{\text{adjoint}\left(\mathbf{A}\right)}{\det\left(\mathbf{A}\right)} \tag{14}$$

The adjoint of matrix $\mathbf{A}$ is formed by the calculating the determinant of the cofactor matrix of each element. A total of twenty four terms from equation (1) was output in order to study the effect of each of the terms on vorticity production and transport.

IV. Results

A. Flowfield

The structure of the flow for circular injectors has been briefly discussed in an earlier section. For injection through a diamond orifice, the interaction shock generated is not as strong as the one generated by a circular orifice because of the streamlined nature of the injector port. Figure 5 shows normalized pressure contours along the tunnel floor and on a transverse plane. The high pressure region downstream of the shock is distinctly visible on both planes. Although the shock strength is comparatively smaller, it still manages to separate the flow ahead of the diamond injector, creating a lambda shock as shown in Fig. 6. At the leading edge the lambda shock merges with the bow shock within a short distance in the axial direction (+ x). However, as we move in the lateral direction (± z), the distance the lambda shock extends in the axial direction a considerable distance before it interacts with the bow shock increases as shown in Fig. 5. It can also be seen that part of this lambda shock never interacts with the bow shock.

The injectant fluid undergoes Prandtl-Meyer expansion as it exits the jet orifice. The expansion terminates in a barrel shock structure. Figures 7(a), 7(b) and 7(c) show the structure of the shock produced by diamond injectors. The shock no longer resembles the "barrel" structure encountered in circular injectors. It is now similar in shape to a wedge or a slice of a blunt body. This "wedge" shock exhibits axis-switching; i.e., it expands more in the lateral direction than in the axial direction. This phenomenon has been observed in experiments[19]. This is very evident at the trailing edge of the jet orifice as the shock expands and forms a "V" shaped normal (to the freestream flow direction) shock; this is analogous to a Japanese *sensu* (fan). As discussed later, this shock shape produces potentially favorable flow structures. In comparison, the barrel shock shape for the circular injector is shown in Fig. 8(a), 8(b) and 8(c). This does not exhibit the *sensu* structure found in the diamond injector shock.

The freestream flow moves over the top surface of the barrel shock and encounters the start of the shear layer. This causes a secondary shock to be formed as shown in both Fig. 5 and Fig. 6. A shear layer having large scale structures is generated by the interaction between the jet fluid and the freestream fluid. These large scale structures create additional shock waves that coalesce with the recompression shock as shown in Fig. 6.

A study of streamlines in the region of the barrel shock reveals interesting flow features. The separation produced by the strong bow shock creates a horseshoe shaped vortex that wraps around the injector. This wrapping of the vortex extends the lambda shock as discussed previously. The horseshoe vortex (red streamlines) is composed of fluid from the inner regions of the freestream boundary layer. The outer regions of the boundary layer "swoop" down behind the horseshoe vortex and flow around the barrel shock as shown in Fig. 9 (yellow streamlines). Downstream of the *sensu* portion of the barrel shock shown in Fig. 7 is a region of low pressure akin to a bluff body. This causes part of the swooping fluid to lift off the floor and move behind the barrel shock. This interacts with the jet fluid as it turns in the freestream direction at the Mach disk [Fig. 10]. The shearing mechanism between the jet fluid and the boundary layer fluid in this region is the likely reason for formation of the transverse counter rotating vortex pair (TCVP). The eventual motion of this vortex pair, as indicated in Fig. 10, shows a structure similar to an "8". It was also observed that a part of the jet fluid from the leading and trailing edges enter the TCVP making it a potentially ideal flame holder, one that was created using gas dynamic effects. This type of flame holder has the advantage of being off the wall and hence avoids thermal effects induced by cavity flame holders. Also, the structure was found to be very steady, when instantaneous and time averaged DES results were compared.

For the circular injector geometry, the separation region is larger as inferred from surface pressure plots of Fig. 8. The extended lambda shock can also be seen in the geometry. The barrel shock does not exhibit axis switching behavior since the orifice is axisymmetric. For the diamond injector, we saw that the axis switching phenomenon couple with normal injection was the cause for formation of the barrel shock with a *sensu* shaped trailing edge. Absence of this phenomena leads to the formation of a barrel shock whose railing edge is inclined in the downstream direction. The streamline behavior around the barrel shock is similar to that of the diamond jet configuration. However, as the boundary layer streamlines move up behind the barrel shock, the inclined shape of the shock nearly aligns these streamlines back into the freestream flow direction [Fig. 11(a), 11(b)]. A pronounced Mach disk can also be seen in Fig. 11(b). The inclined barrel shock downstream surface coupled with realignment of the lifting boundary layer fluid seems to be the likely cause for the absence of a coherent transverse counter rotating vortex pair. There is, however, a semblance of TCVP for this geometry, the cores of which seem to be aligned in the axial direction.

B. Vorticity Transport Analysis.

A FORTRAN program was written to analyze the vorticity transport process using the compressible vorticity transport equation [Eq. (1)]. The technique used to evaluate necessary gradients is presented in a previous section.

This equation involves second and third order derivatives of velocity, and therefore caused noise to be introduced into the postprocessing. However, this does not preclude the use of this technique to identify mechanisms contributing towards vorticity evolution.

Figures 12(a) and 13(a) show contours of vorticity convection. Two perpendicular planes are shown; (a) along the tunnel centerline and (b) cross sectional plane immediately downstream of the jet and passing though the TCVP. The barrel shock structure for both geometries is clearly visible. The strongest regions of vorticity transport seem to be at the leading and trailing edges of the jet orifice. The likely reason for the leading edge peak is the presence of the recirculation region. Also significant interaction takes place between the exiting jet fluid and the boundary layer of the freestream. Leading edge stirring was observed in the diamond injector case which may explain higher values seen in Fig. 12(a) as compared to Fig. 13(a).

Compressibility effects are shown in Fig. 12(b) and 13(b). They isolate the strength of the barrel shock. It is apparent that the barrel shock in the case of circular injectors seems to have larger compressibility effects as compared to the diamond jet barrel shock. Since the jet fluid has to pass through these shocks, stronger shocks might lead to weaker penetration. It was observed in experiments[19] that downstream penetration was higher for diamond injectors compared to circular injectors. The strongest sections of the barrel shock for the circular injector seems to occur at the leading edge and the Mach disk.

The predominant effect in the region occupied by the TCVP occurs due to vortex stretching [Fig. 12(c) and 13(c)]. Peak values of vortex stretching are seen in Fig. 12(c) in the entire region behind the barrel shock while in 13(c), peak values occur near the Mach disk. This is consistent with the vortex pairs seen for the diamond and circular injectors seen in Fig. 10 and Fig. 11. Two mechanisms that may account for the contribution of vortex stretching were identified. The shape of the TCVP on the downstream side resembles a pair of cones, with their apexes pointing in the downstream direction. Fluid is ejected out of the TCVP through these structures. A secondary mechanism within the TCVP ejects fluid in the lateral direction. The shearing action between the jet fluid and the freestream fluid that occurs near the leading edge of the jet is also highlighted in the contours. This shear region can also be seen just above the barrel shock and under the bow shock in Fig. 6.

Baroclinic torque, the mechanism by which vorticity is generated across shocks, has little impact on the TCVP structure as seen in Fig. 12(d). The strongest region of baroclinic torque generation occurs at the Mach disk.

The effects of turbulent anisotropic torque can be seen in Fig. 12(e) and 13(e). The shearing action between the jet fluid and the lifting boundary layer fluid was suggested as an important mechanism in the formation of the TCVP. The region of this shearing action corresponds to the peaks in the contours of turbulent anisotropic torque. Other peak regions include the shear layer near the jet leading edge.

V. Conclusion

Detached eddy numerical simulations were conducted to study the role of the barrel shock in controlling secondary motion associated with gaseous injection of an underexpanded jet through circular and 15-degree half-angle diamond injectors into a hypersonic freestream. Results were post processed using visualization tools and in-house analysis software. A study of shock structures and streamlines was conducted to understand the effects of the barrel shock shape on the flowfield. A new transverse counter rotating vortex pair was identified just downstream of the barrel shock. This vortex pair has the potential to act as a scramjet flame holder. Further analysis was conducted to identify contributions to vorticity evolution by mechanisms such as compressibility, vortex stretching, baroclinic torque etc. It was found that the contribution of vortex stretching towards the TCVP evolution was significant. Two mechanisms that may account for the contribution of vortex stretching were identified. Anisotropic turbulent torque is predominant in the interaction region between the jet fluid and the boundary layer fluid near the Mach disk.

Acknowledgments

The authors would like to acknowledge Drs. Forsythe and Tomaro of Cobalt Solutions, LLC and Dr. Shahyar Pirzadeh of LARC for their help with Cobalt execution and grid adaption. Generous amounts of supercomputer time were allotted for this work by the Aeronautical Systems Center for which the authors express their gratitude. The authors thank Dr. John Schmisseur from the Air Force Office of Scientific Research for sponsoring this research.

References

[1] Beach, H., and Blankson, I., Jr., "Prospects for Future Hypersonic Air-Breathing Vehicles," AIAA-91-5009, Dec. 1991.

[2] Freeman, D. C., Jr., Reubush, D. E., McClinton, C. R., Rausch, V. L.,and Crawford, J. F., "The NASA Hyper-X Program," *48th International Astronautical Congress*, NASA-97-48IAC-DCF, Turin, Italy, Oct. 1997.

[3] Heiser, W., and Pratt, D., *Hypersonic Airbreathing Propulsion*, AIAA Education Series, AIAA, WashingtonDC, 1994, pp. 277–378.
[4] V. Khorunzhenko, D. Roupassov and A. Starikovskii, "Hypersonic Flow and Shock Wave Structure Control by Low Temperature Nonequilibrium Plasma of Gas Discharge," AIAA 2002-3569, July, 2002.
[5] V. Khorunzhenko, D. Roupassov and A. Starikovskii, "Hypersonic Shock Wave — Low Temperature Nonequilibrium Plasma Interaction," AIAA 2003-5048, July, 2003.
[6] N. Anikin, E. Mintoussov, S. Pancheshnyi, D. Roupassov, A. Starikovskii and V. Sych, "Nonequilibrium Plasmas and its Application for Combustion and Hypersonic Flow Control," AIAA 2003-1053, January, 2003.
[7] Sergey B. Leonov, Valentin A. Bityurin, "Hypersonic/Supersonic Flow Control by Electro-Discharge Plasma Application," AIAA 2002-5209
[8] David W. Riggins, H. F. Nelson, "Hypersonic Flow Control Using Upstream Focused Energy Deposition," *AIAA Journal*, Vol. 38, No. 4., 1999, pp. 723-725.
[9] D. Knight, "Survey of Aerodynamic Flow Control at High Speed By Energy Deposition," AIAA 2003-0525, January, 2003.
[10] A. L. Kuranov, E. G. Sheikin, "Magnetohydrodynamic Control on Hypersonic Aircraft Under "Ajax" Concept," *Journal of Spacecraft and Rockets*, Vol. 40, No. 2., 2003, pp. 174-182.
[11] S. O. Macheret, M. N. Shneider, and R. B. Miles, "Magnetohydrodynamic and Electrohydrodynamic Control of Hypersonic Flows of Weakly Ionized Plasmas," AIAA 2002-2249, May, 2002.
[12] L. S. Jacobsen, S. D. Gallimore, J. A. Schetz, and W. F. O'Brien, "Improved Aerodynamic-Ramp Injector in Supersonic Flow," *Journal of Propulsion and Power*, Vol. 19, No. 4, 2003, pp. 663-673.
[13] B. Auvity, M. Etz, M. Huntley, Pingfan P. Wu and A. J. Smits,"Control of Hypersonic Boundary Layers by Helium Injection," AIAA 2000-2322, June, 2000.
[14] Bruno Auvity, Michael R. Etz, and Alexander J. Smits," Effects of Transverse Helium Injection on Hypersonic Boundary Layers," *Physics of Fluids*, Vol. 13, No. 10., 2001, pp. 3025-3032.
[15] Davis, D. L. and Bowersox, R. D. W., "Stirred Reactor Analysis of Cavity Flame Holders for Scramjets," AIAA 97-3274, July, 1997.
[16] Davis, D. L. and Bowersox, R. D. W., "Computational Fluid Dynamics Analysis of Cavity Flame Holders for Scramjets," AIAA 97-3270, July, 1997.
[17] Zukowski, E. and Spaid, F., "Secondary Injection of Gases into a Supersonic Flow," *AIAA Journal*, Vol. 2, No. 10, 1964, pp. 1697-1705.
[18] Schetz, J. and Billig, F., "Penetration of Gaseous Jets Injected into a Supersonic Stream", *Journal of Spacecraft and Rockets*, Vol. 3, No. 11, 1966, pp. 1658-1665.
[19] Tomiaka, S., Jacobsen, L., and Schetz, J., "Angled Injection through Diamond Orifices into a Supersonic Stream," AIAA 2001-1762, April, 2001.
[20] Bowersox, R., Fan, H. and Lee, D., Gaseous Injection through Diamond Orifices into a Mach 5.0 Freestream at Various Incidence," *Journal of Propulsion and Power*, Vol. 20, No. 2, 2004, pp. 280-287.
[21] Barber, M. Schetz, J., and Roe, L., "Normal Sonic Helium Injection Through a Wedge-Shaped Orifice into a Supersonic Flow," *Journal of Propulsion and Power*, Vol. 13, No. 2, 1997, pp. 257-263.
[22] Champigny P. and Lacau R. G., "Lateral Jet Control for Tactical Missiles," AGARD Special Course on Missile Aerodynamics, June 1994.
[23] Pirzadeh, S., "Three-Dimensional Unstructured Viscous Grids by the Advancing-Layers Method," *AIAA Journal*, Vol. 34, No. 1, January 1996, pp. 43-49.
[24] W. Z. Strang, R. F. Tomaro and M. J. Grismer., "The Defining Methods of Cobalt60: A Parallel, Implicit, Unstructured Euler/Navier-Stokes Flow Solver," AIAA 1999-0786.
[25] Menter, F. R., "Two-Equation Eddy-Viscosity Turbulence Models for Engineering Applications," *AIAA Journal*, Vol. 32, No. 8, August 1994, pp. 1598-1605.
[26] Strelets, M., "Detached Eddy Simulation of Massively Separated Flow," AIAA 01-0879, January 2001.
[27] Mingyu Sun, "Numerical and Experimental Studies of Shock Wave Interaction With Bodies," Ph.D. Dissertation, Tohoku University, 1998.

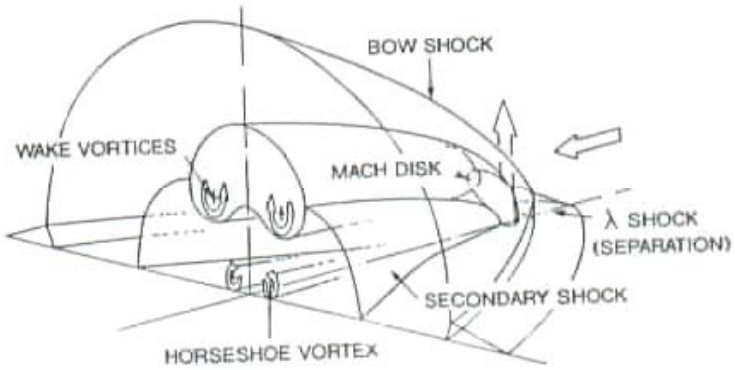

Figure 1. Schematic of Supersonic Jet Interaction Flowfield.

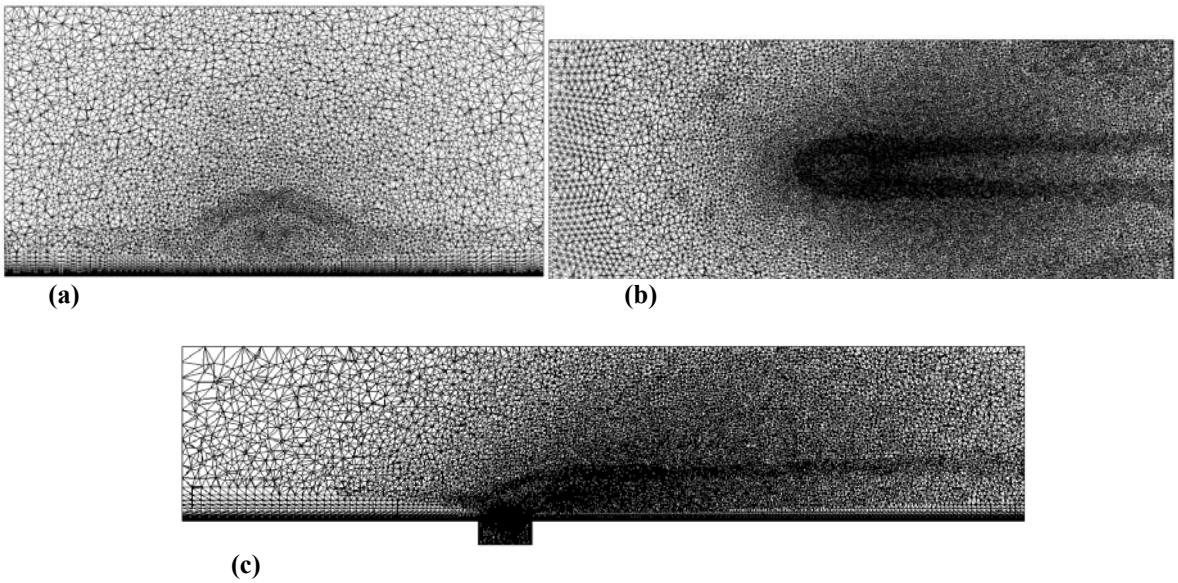

Figure 2. Unstructured Grid

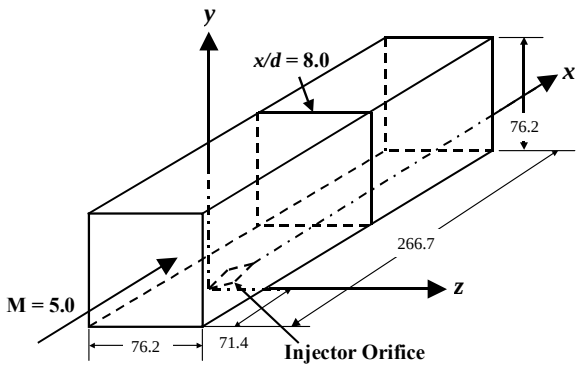

Figure 3 . Physical Domain.

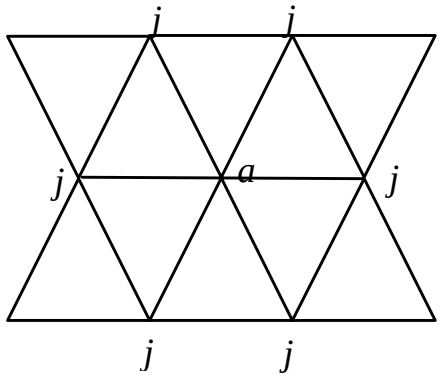

Figure 4. Current Grid Point, *a*, and neighbors *j*.

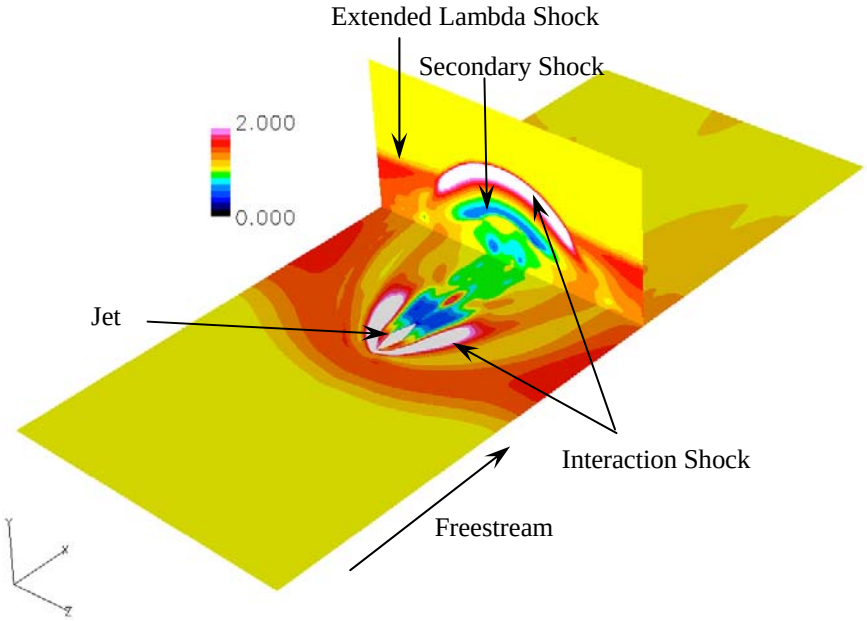

Figure 5. Normalized Pressure Contours (p/p_∞) – Diamond Injector.

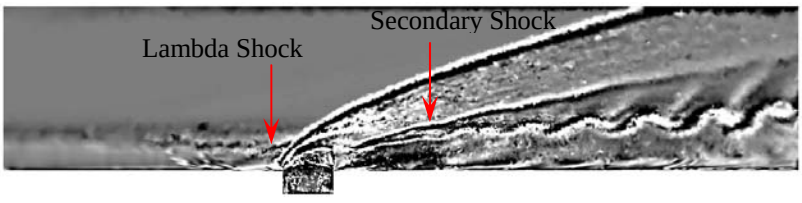

Figure 6. Shadowgraph Showing Lambda Shock – Diamond Injector.

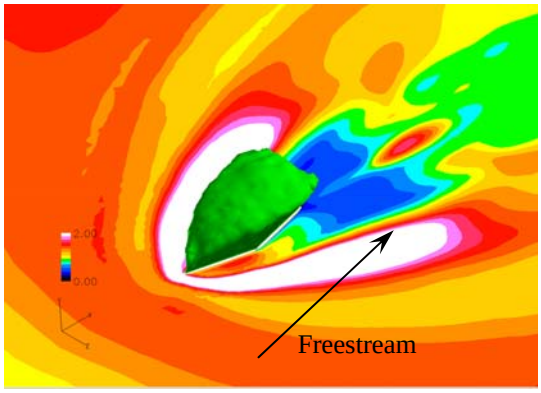

(a)

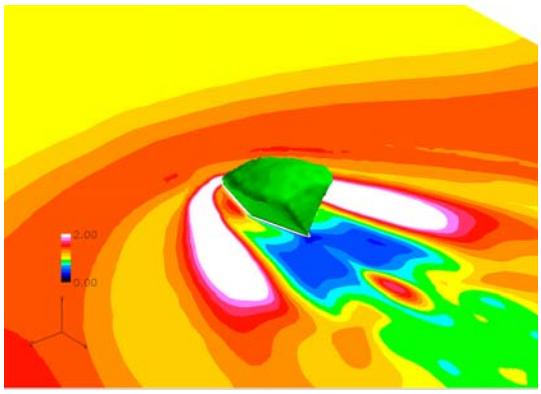

(b)

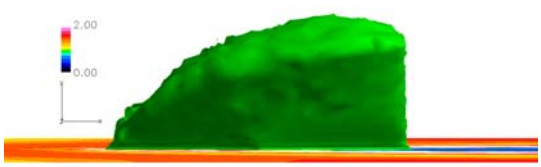

(c)

Figure 7. Barrel Shock Structure – Diamond Injector.

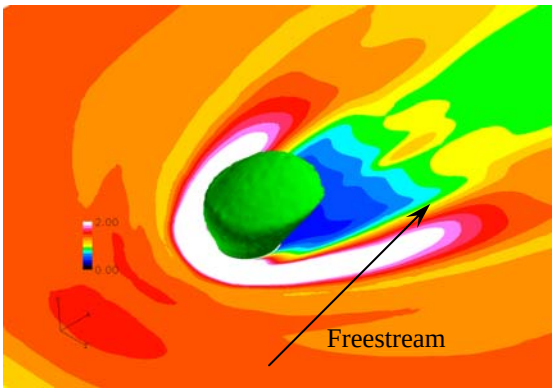

(a)

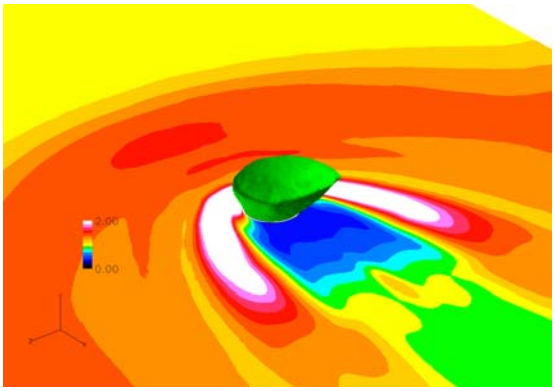

(b)

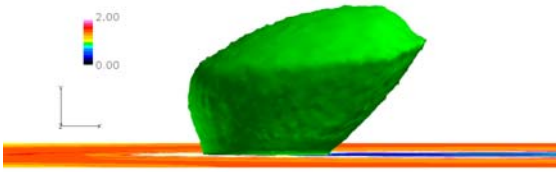

(c)

Figure 8. Barrel Shock Structure – Circular Injector.

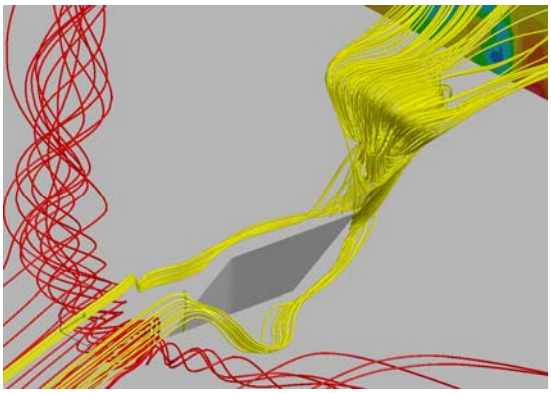

Figure 9. Boundary Layer Streamlines – Diamond Injector.

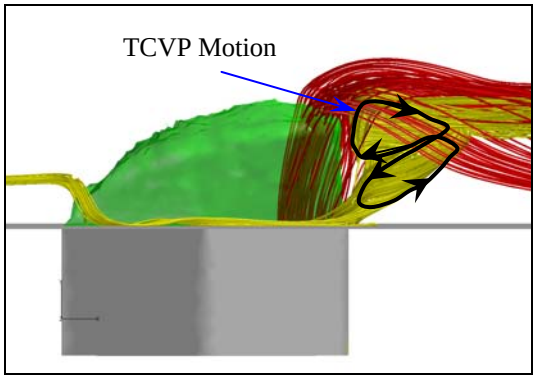

Figure 10. Boundary Layer Streamlines – Diamond Injector.

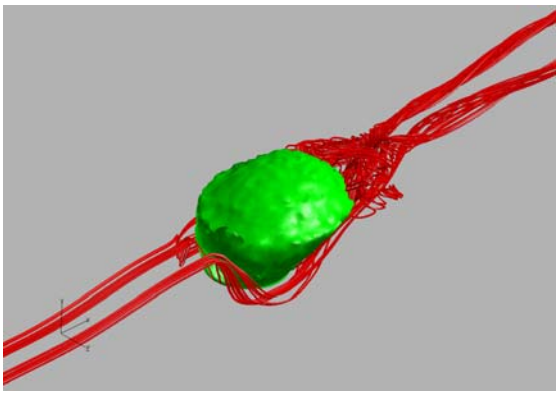

(a)

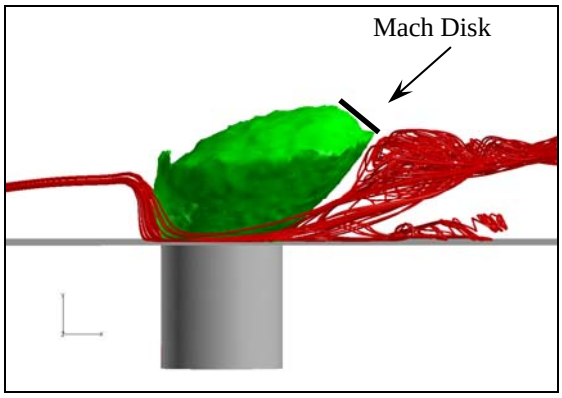

(b)

Figure 11. Streamlines Around Barrel Shock – Circular Injector.

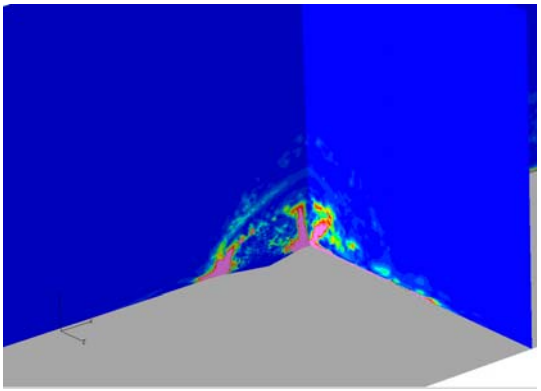

(a) Convection

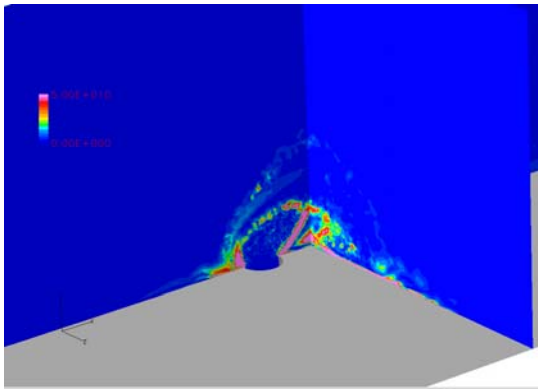

(a) Convection

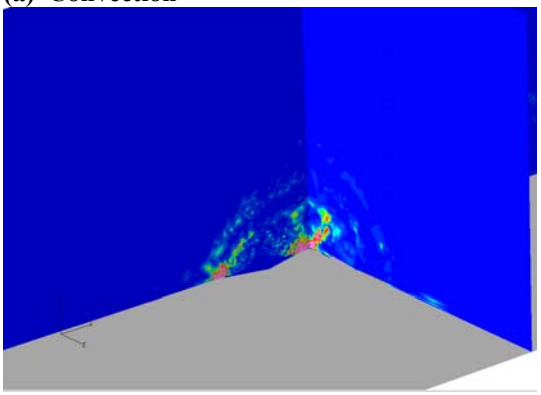

(b) Compressibility

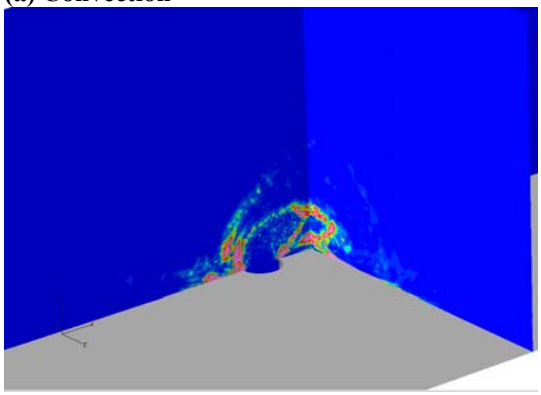

(b) Compressibility

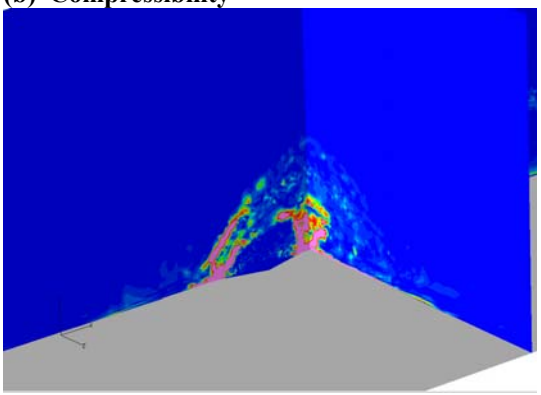

(c) Vortex Stretching

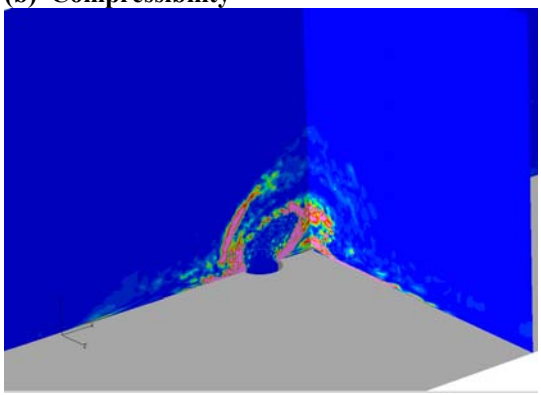

(c) Vortex Stretching

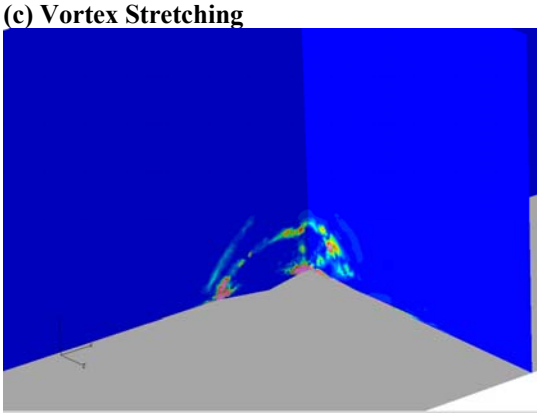

(d) Baroclinic Torque

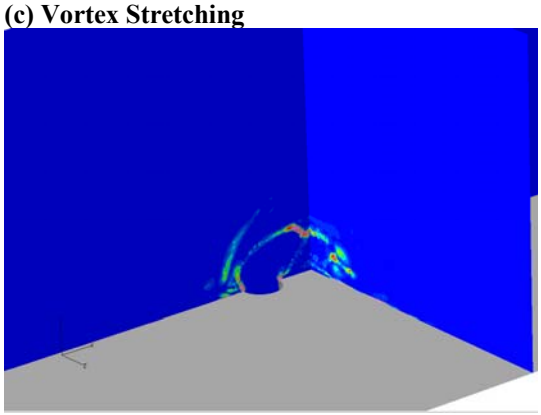

(d) Baroclinic Torque

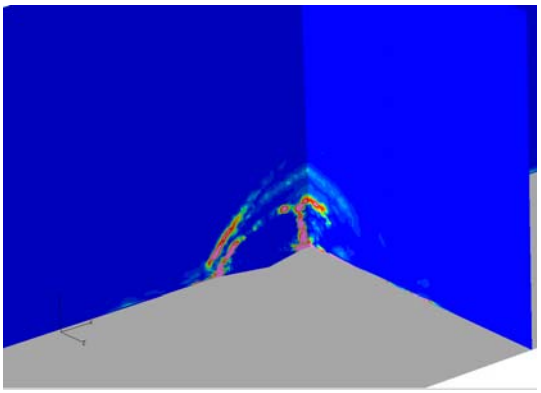

(e) Turbulent Anisotropic Torque

Figure 12. Vorticity Evolution Analysis – Diamond Injector.

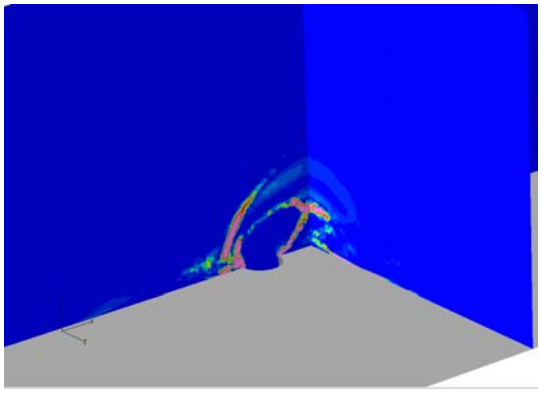

(e) Turbulent Anisotropic Torque

Figure 13. Vorticity Evolution Analysis – Circular Injector.